Supplementary information for

Data-driven super-resolution optoacoustic imaging via physically encoded signal acquisition

Irene Pi – Martín[1], Daniil Nozdriukhin[2], Alejandro Cebrecos[1], Juan José García – Garrigós[1], Daniel Razansky[2], Xose Luis Dean – Ben[2]*.

1 Instituto de Instrumentación para Imagen Molecular (i3M), CSIC – Universitat Politècnica de València, Camino de Vera S/N, 46022, Valencia, Spain

2 Institute for Biomedical Engineering, Department of Information Technology and Electrical Engineering, ETH Zurich, Zurich, Switzerland

* email: xl.deanben@pharma.uzh.ch; xdeanben@ethz.ch

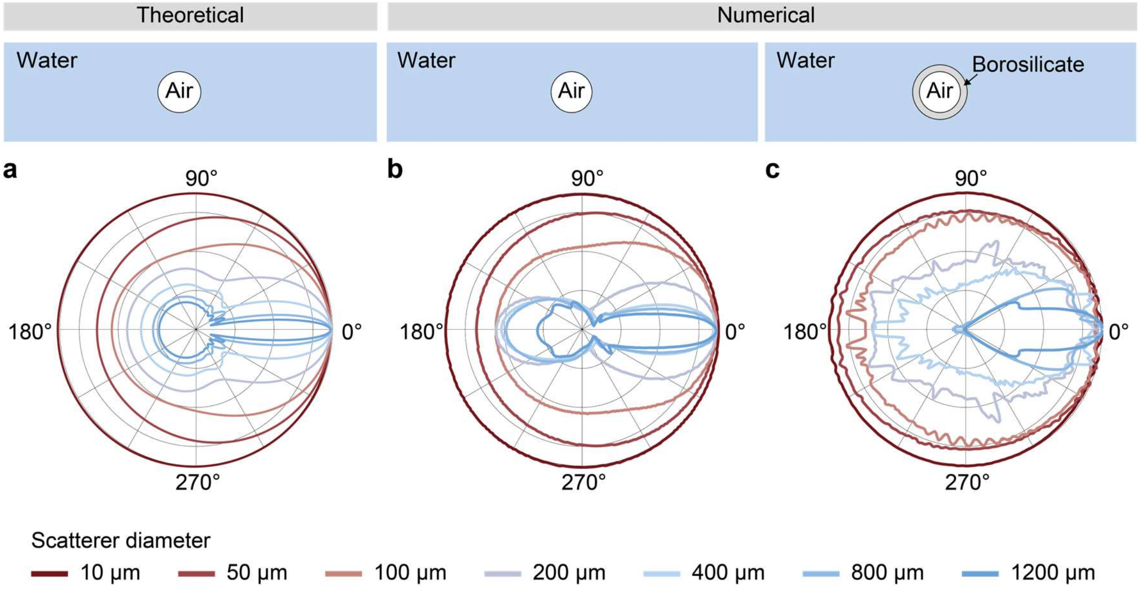

Supplementary Figure 1. Acoustic scattering regimes. (a) Theoretical acoustic scattering produced by cylindrical scatterers of different sizes, spanning regimes from Rayleigh to Mie scattering. (b) Numerically computed acoustic scattering from air cylindric scatterers, considering a central frequency of 5 MHz and 80% bandwidth (BW). (c) Numerically computed acoustic scattering from scatterers consisting of air enclosed by a borosilicate wall, under the same excitation conditions (5 MHz and 80% BW). The presence of the wall introduces an additional impedance contrast and structural resonance effects, leading to a more complex response that better resembles the experimental situation.

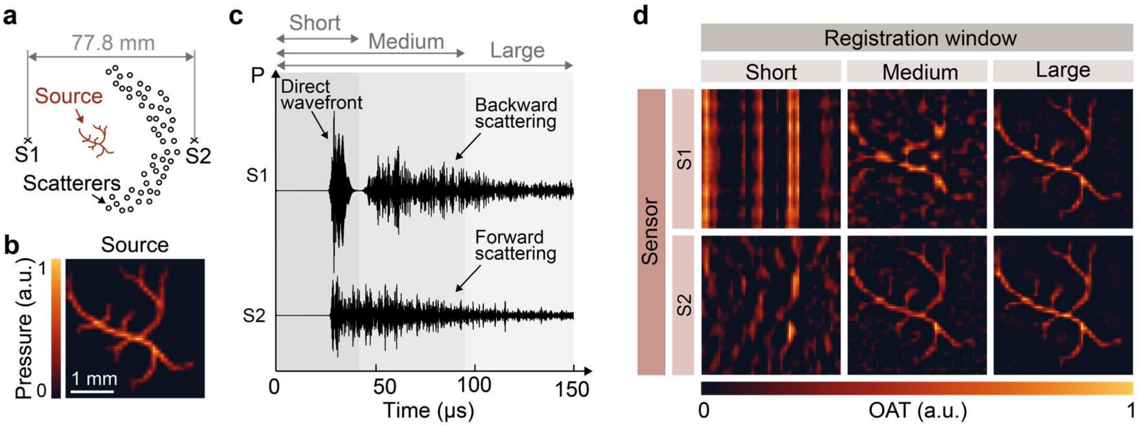

Supplementary Figure 2. Physical encoding in model-based optoacoustic reconstruction. (a) Schematic of the numerical validation framework for model-based optoacoustic (OA) tomography employing a single sensor (S1 or S2) and an acoustically scattering medium that physically encodes the OA signals. (b) Initial pressure distribution employed as the OA source in the numerical simulation. (c) S1 and S2 recorded signals when the sensors are positioned as indicated in panel (a). (d) Model-based reconstructions based on the signals recorded by sensors S1 (top row) and S2 (bottom row), using recording windows of increasing duration (short, medium, and long) from left to right, as indicated in (c).

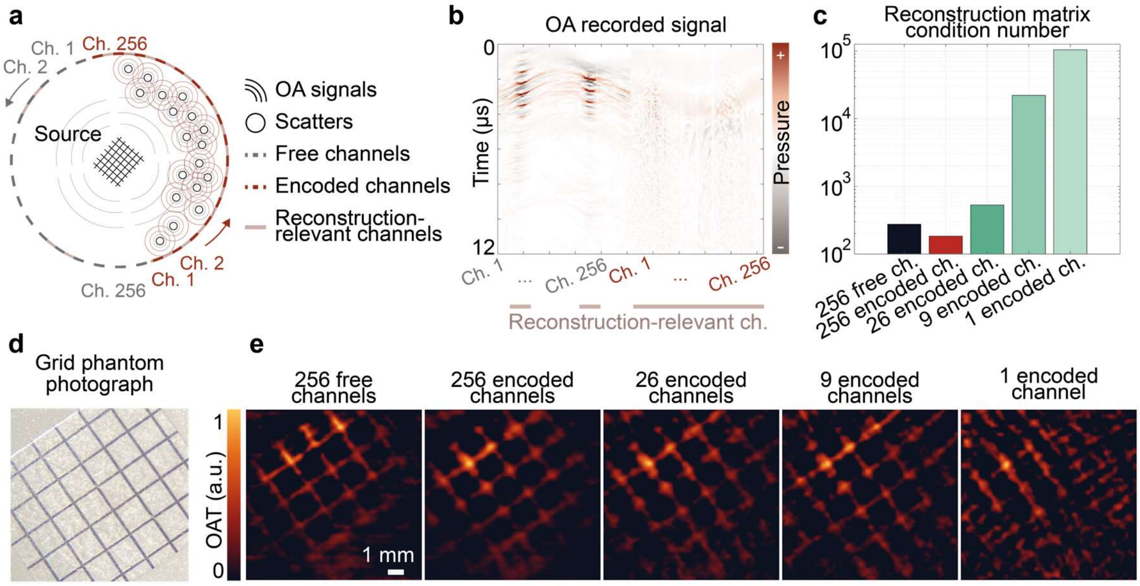

Supplementary Figure 3. Expansion of reconstruction-relevant channels via scatter-mediated signal redirection in optoacoustic tomography. (a) Schematic of the grid phantom experiment. The generated OA signals exhibit maximum perpendicular directivity, restricting the relevant reconstruction channels to two narrow sectors in the scatter-free half ring (gray). The scatterers redirect the signals, expanding them throughout the encoded half ring (red). (b) OA signals recorded in the experiment shown in panel (a). (c) Reconstruction matrix condition number for 256 scatter-free channels, and 256, 26, 9, and 1 encoded channels. (d) Photograph of the grid phantom. (e) OAT reconstructions using the 256 scatter-free channels, and 256, 26, 9, and 1 encoded channels.

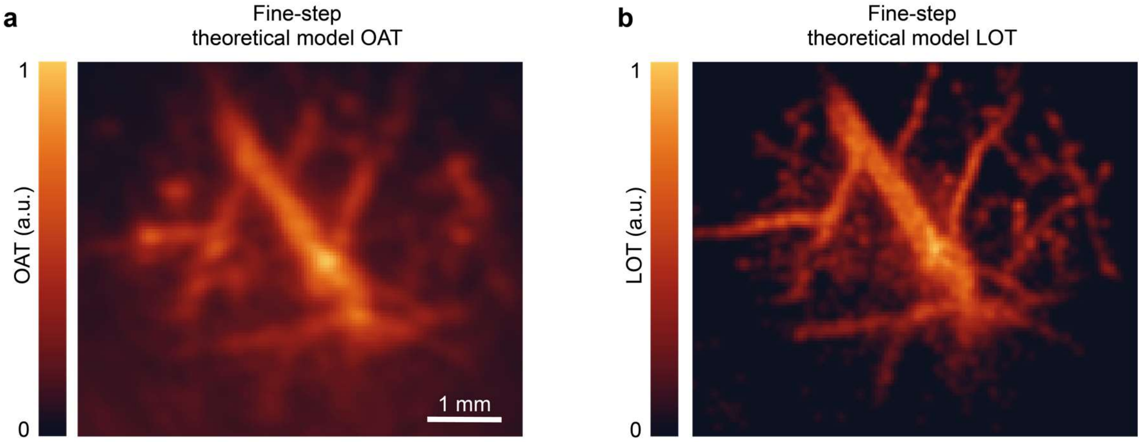

Supplementary Figure 4. Standard optoacoustic reconstruction method. (a) OAT image reconstructed using the theoretical fine–step (36.1 μm) free half-ring model, the OA signal originates from the laser excitation of the mouse vasculature prior to contrast agent injection. (b) LOT image based on reconstructions performed with the fine–step free half-ring theoretical model.

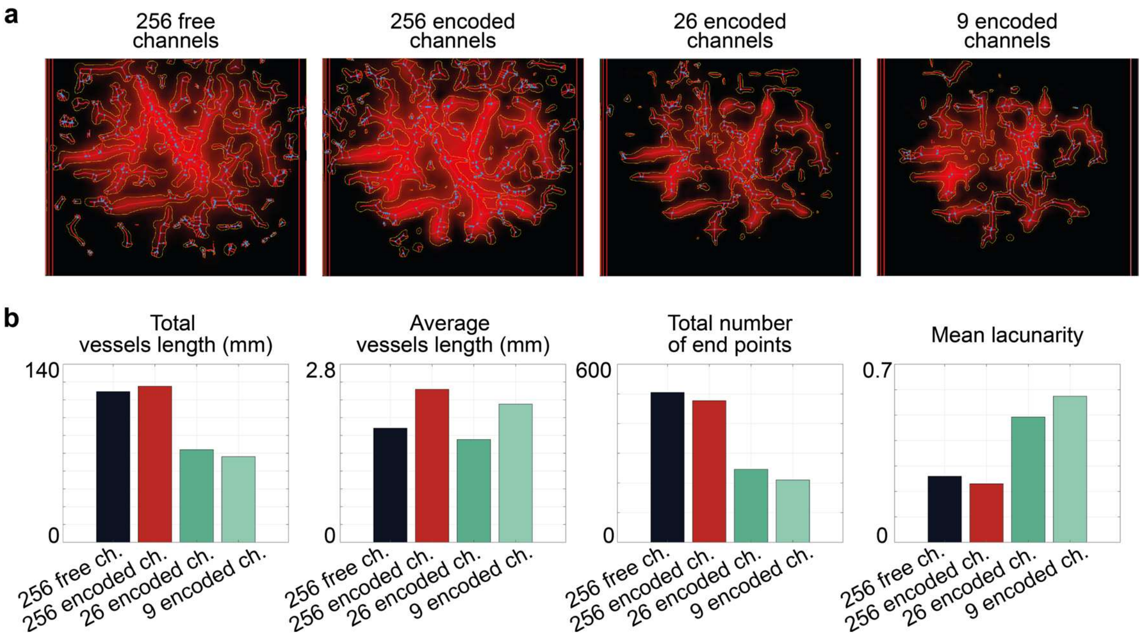

Supplementary Figure 5. Angiographic analysis. (a) Vascular network analysis using AngioTool, showing vessel traces (red lines) and junctions (blue points) for different reconstruction configurations. From left to right: 256 free channels, and 256, 26, and 9 encoded channels. (b) Quantitative angiogenesis-related metrics (from left to right: total vessel length, mean vessel length, total number of endpoints, and mean lacunarity) derived from the vascular analysis shown in panel (a).

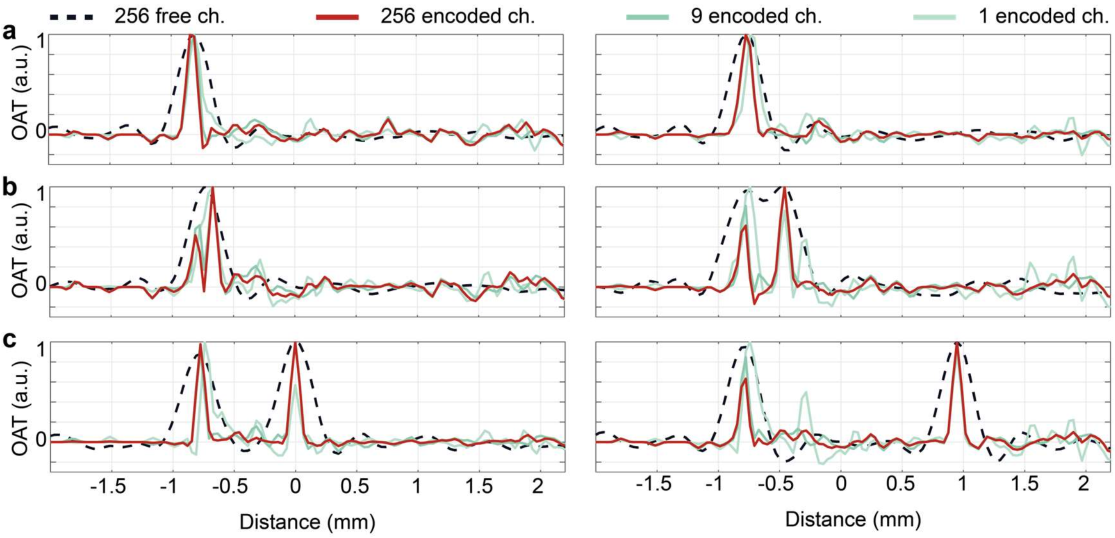

Supplementary Figure 6. Resolution of closely spaced microparticles using self-calibrated optoacoustic reconstruction. One-dimensional self-calibrated reconstructed profiles for two microparticles flowing through a tubing, obtained using standard optoacoustic tomography (OAT) reconstruction and a self-calibrated model based on encoded channels. (a) The inter-particle distance is below the system's resolving capability, resulting in an unresolved, merged signal. (b) With a moderate increase in inter-particle separation, partial resolution is achieved, and the two microparticles become distinguishable using the self-calibrated approach. (c) At larger separations, the microparticles are fully resolved as two distinct peaks.

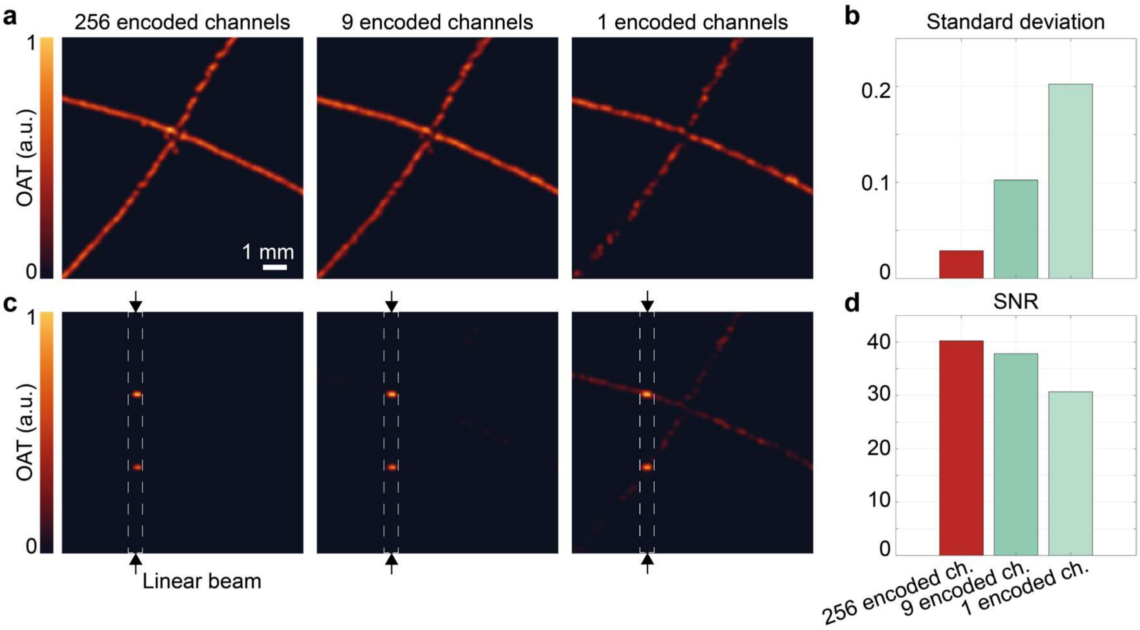

Supplementary Figure 7. Self-calibrated phantom. (a) Cross-shaped phantom consisting of two intersecting surgical sutures embedded in uniformly illuminated agar, reconstructed using 256, 9, and 1 encoded channels with a self-calibrated model-based approach. (b) Standard deviation maps corresponding to the three reconstructions shown in panel (a). (c) Reconstructions obtained with 256, 9, and 1 channels under line-beam excitation, where the cross is illuminated only at two points, generating two localized optoacoustic (OA) point sources. (d) Signal-to-noise ratio (SNR) for the three cases shown in (c), where the signal is defined as the OA point sources and the noise corresponds to the remaining signal within the calibrated region (i.e., the cross).

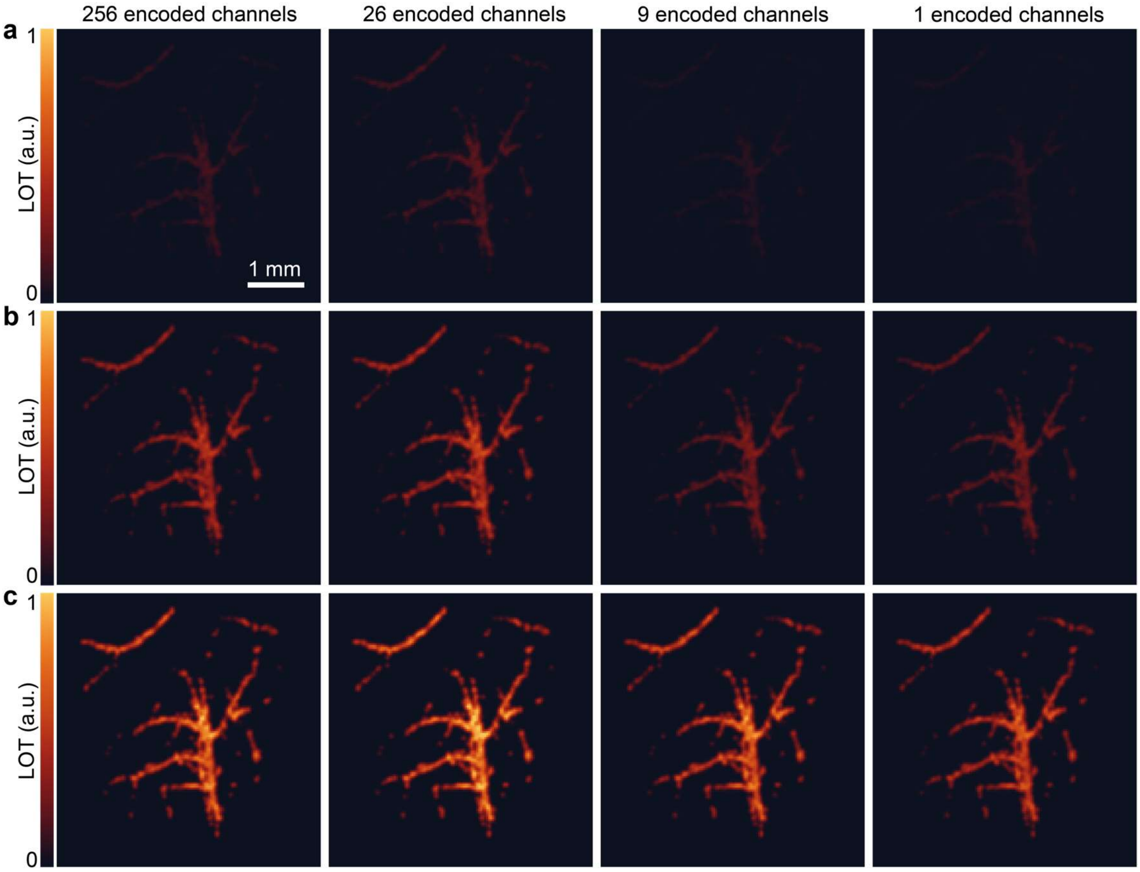

Supplementary Figure 8. *In vivo* localization optoacoustic tomography (LOT) reconstructions obtained using the self-calibrated method. Columns show results reconstructed with 256, 26, 9, and 1 encoded channels (from left to right). Rows correspond to different acquisition times: (a) short acquisition time (400 stacked frames), (b) intermediate acquisition time (900 stacked frames), and (c) long acquisition time (1500 stacked frames).